Magnetotransport studies of mobility limiting mechanisms in undoped Si/SiGe heterostructures

X. Mi,[1] T. M. Hazard,[1] C. Payette,[1] K. Wang,[1,*] D. M. Zajac,[1] J. V. Cady,[1] and J. R. Petta[1,2]
[1]*Department of Physics, Princeton University, Princeton, New Jersey 08544, USA*
[2]*Department of Physics, University of California, Santa Barbara, California 93106, USA*
(Received 19 March 2015; revised manuscript received 2 June 2015; published 16 July 2015)

We perform detailed magnetotransport studies on two-dimensional electron gases (2DEGs) formed in undoped Si/SiGe heterostructures in order to identify the electron mobility limiting mechanisms. By analyzing data from 26 different heterostructures, we observe a strong correlation between the background oxygen concentration in the Si quantum well and the maximum mobility. The highest-quality wafer supports a 2DEG with mobility $\mu = 160\,000$ cm^2/Vs at a density $n = 2.17\times10^{11}$/cm^2 and exhibits a metal-to-insulator transition at a critical density $n_c = 0.46\times10^{11}$/cm^2. We extract a valley splitting $\Delta_v \sim 150$ μeV at a magnetic field $B = 1.8$ T. These results provide evidence that undoped Si/SiGe heterostructures are suitable for the fabrication of few-electron quantum dots.

DOI: 10.1103/PhysRevB.92.035304 PACS number(s): 73.21.Fg, 73.21.La, 85.30.De

I. INTRODUCTION

The development of silicon quantum devices has gained considerable momentum due to reports of exceptionally long quantum coherence times [1]. Its naturally abundant isotope, ^{28}Si, carries zero nuclear spin, reducing hyperfine-induced spin dephasing [2–4]. Small spin-orbit coupling is also beneficial for spin qubits [4]. Following work in GaAs quantum dots, early experimental efforts were made towards fabricating Si quantum dots in modulation-doped Si/SiGe heterostructures, where the n-type dopant layer is separated from the Si quantum well (QW) by a setback distance ranging from 5 to 20 nm [5–8]. Doped devices were challenging to operate in the few-electron regime, unstable [8], and sometimes suffered from gate leakage [5,7].

It is now widely accepted that the elimination of the n-type dopant layer decreases the Coulomb disorder in the QW, and reduces hysteresis and gate leakage [9,10]. Recent experiments on quantum dots made in undoped Si/SiGe QWs [9–12] have consistently reached the single-electron regime and demonstrated inhomogeneous spin dephasing times $T_2^* = 360$ ns in naturally abundant Si, a substantial increase compared to GaAs spin qubits [3,12]. Further improvement of the Si/SiGe QW system may be feasible if the remaining mobility limiting mechanisms are identified [13,14].

The dominant scattering sources can be identified from measurements of the carrier mobility μ as a function of two-dimensional electron gas (2DEG) charge density n and measurements of the quantum lifetime τ_q [13,15]. For example, scattering from remote impurities [13] is predicted to result in a power-law dependence $\mu \propto n^{1.5}$. Such experiments have been extensively performed for GaAs/AlGaAs heterostructures [16–19], Si metal-oxide-semiconductor field-effect transistors (MOSFETs) [20], and doped Si/SiGe heterostructures [21–23]. Similar measurements of undoped Si/SiGe heterostructures are scarce [23,24].

To thoroughly investigate the mobility limiting mechanisms in undoped Si/SiGe QWs, we report a series of systematic magnetotransport measurements. By examining 26 different heterostructures, we identify a strong correlation between background oxygen concentration in the QW and maximum mobility. These results indicate that significant enhancements in Si/SiGe mobility might be obtained through more careful control of background contamination during heterostructure growth.

II. SILICON GERMANIUM HETEROSTRUCTURES

The samples were grown at Lawrence Semiconductor Research Laboratory using chemical vapor deposition [Fig. 1(a)]. Relaxed buffers of $Si_{1-x}Ge_x$ are first grown on 6-inch-diameter Czochralski process Si substrates with 10–20 ohm cm resistivity, varying x from 0 to 0.3 over a thickness of 3 μm. A 1-μm-thick layer of $Si_{0.7}Ge_{0.3}$ is grown on the virtual substrate before it is polished. The relaxed buffer substrate has threading dislocation densities on the order of 10^6/cm^2, as determined by cross-sectional transmission electron microscopy. The wafers are completed by growing a 225-nm-thick $Si_{0.7}Ge_{0.3}$ layer, followed by a strained Si QW, a $Si_{0.7}Ge_{0.3}$ spacer layer, and a protective Si cap. All heterostructure layers are grown at a temperature of 650 °C. The $Si_{1-x}Ge_x$ layers are grown with H_2SiCl_2 and GeH_4 at a rate of 60–65 nm per min. The Si Cap is grown with H_2SiCl_2 at a rate of 2 nm per min and the Si QW is grown with SiH_4 at a rate of 9–10 nm per min. We investigate heterostructures with Si cap thicknesses of 2 and 4 nm, $Si_{0.7}Ge_{0.3}$ spacer layer thicknesses $h = 20$, 30, 40, and 50 nm, and Si QW thicknesses of 5, 8, and 11 nm.

Hall bars are fabricated on each of the 26 wafers, with the geometry shown in Fig. 1(b). We first use atomic layer deposition to grow an Al_2O_3 gate dielectric on top of the Si cap. We then evaporate Cr/Au on top of the Al_2O_3 to form a top gate. A positive dc bias is applied to the top gate to accumulate electrons in the QW and a 0.1 mV, 17 Hz ac voltage excitation is applied between the S and D ohmic contacts. The longitudinal voltage V_{xx}, Hall voltage V_{xy}, and source-drain current I_{SD} are simultaneously measured using standard ac lock-in techniques. The 2D longitudinal resistivity, $\rho_{xx} = (V_{xx}/I_{SD})(W/L)$, and Hall resistivity, $\rho_{xy} = (V_{xy}/I_{SD})$, are calculated from the measured voltages and currents. Density n and mobility μ of carrier electrons are calculated

*Present address: Department of Physics, Harvard University, Cambridge, MA 02138, USA.

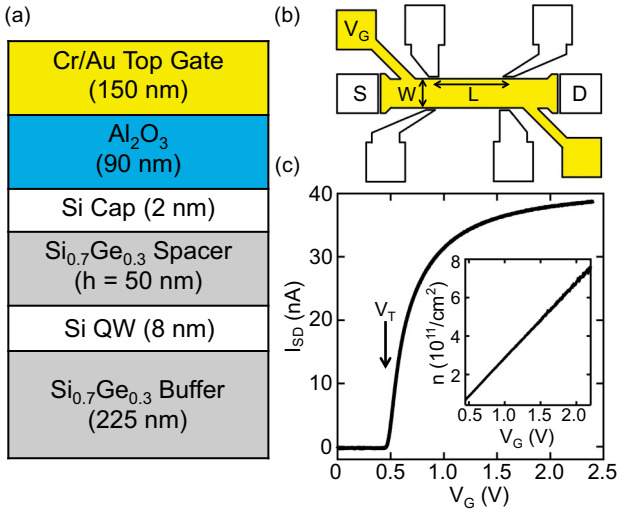

FIG. 1. (Color online) (a) Heterostructure growth profile. (b) Top view of the Hall bar device. The gold region marks the area covered by the top gate. The other six square pads are ^{15}P implanted regions which form ohmic contacts to the electron gas. The Hall bar dimensions are $W = 170\ \mu$m and $L = 375\ \mu$m. (c) A typical "turn-on" curve of the device at $T = 0.35$ K showing I_{SD} as a function of V_G. The threshold voltage is $V_T = 0.45$ V. Inset: n for $V_G > V_T$, before saturation. Dimensions and data shown in (a) and (c) are for wafer 16.

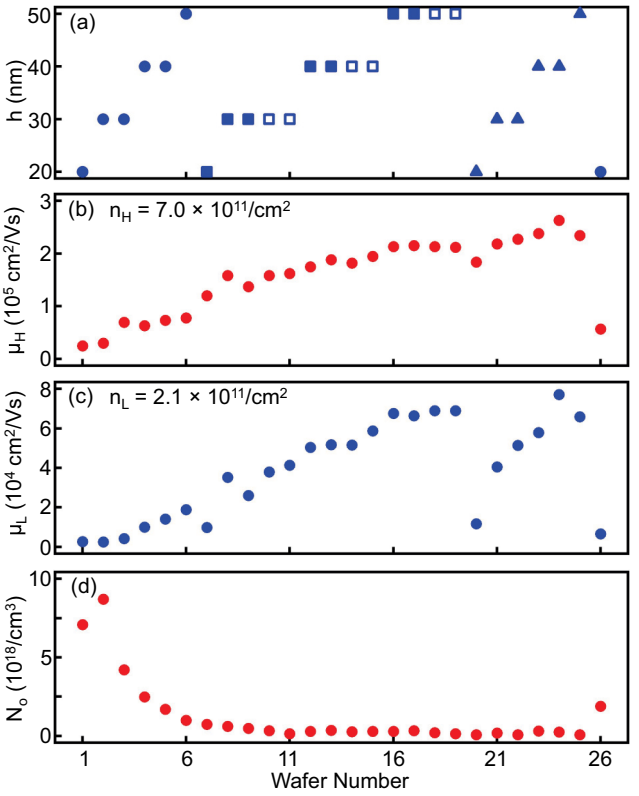

FIG. 2. (Color online) (a) SiGe spacer layer thickness h for wafers 1 through 26. Wafers with solid (empty) symbols have a 2-nm-thick (4-nm-thick) Si cap. QW thicknesses are represented by symbol shapes. Circles: 5 nm; rectangles: 8 nm; triangles: 11 nm. (b) μ_H is the $T = 4.2$ K mobility at $n_H = 7\times10^{11}$/cm^2. (c) μ_L is the $T = 4.2$ K mobility at $n_L = 2.1\times10^{11}$/cm^2. (d) N_o is the concentration of oxygen atoms inside the QW.

according to the Hall formulas $n = B/(e\rho_{xy})$ and $\mu = (1/B)(\rho_{xy}/\rho_{xx})$.

Figure 1(c) displays a typical "turn-on" curve of the Hall bar devices. Zero current flow is observed below a threshold top gate voltage $V_t = 0.45$ V. For $V_G > V_t$, current starts to flow and we observe a linear increase in n with a slope of $dn/dV_G = 3.96\times10^{11}$/cm^2/V. Using relative permittivities $\epsilon_r = 9$ for Al_2O_3 and $\epsilon_r = 13.1$ for $Si_{0.7}Ge_{0.3}$, we calculate $dn/dV_G = 4.00\times10^{11}$/cm^2/V, which is within 1% of the experimental value. At even higher values of V_G (data not shown), electrons start to accumulate at the Al_2O_3/Si cap interface, screening the QW from any further increase in V_G. This causes a saturation of the electron density at a constant value of 8.0×10^{11}/cm^2 for $V_G > 2.5$ V [25].

III. CHARACTERIZATION AT $T = 4.2$ K

Hall bars are first measured at $T = 4.2$ K and $B = 0.1$ T, below the onset of Shubnikov–de Haas (SdH) oscillations. Figure 2(a) shows the spacer layer thickness h for each of the 26 wafers, along with the Si cap thickness and QW width. Recent studies of undoped Si/SiGe structures have shown that remote impurity scattering typically dominates in the low-electron-density regime, whereas both remote impurities and interface roughness dominate at higher electron densities [23,24]. It is therefore helpful to examine electron mobilities in both regimes. Electron mobilities are plotted in Fig. 2(b) for $n_H = 7.0\times10^{11}$/cm^2 and in Fig. 2(c) for $n_L = 2.1\times10^{11}$/cm^2. Surprisingly, the mobilities show a nearly monotonic increase with wafer number, despite the large variation in heterostructure parameters throughout this series of wafers. On top of this trend, abrupt dips in the mobility are observed at wafers 20 and 26.

Secondary ion mass spectrometry (SIMS) analysis was performed on each wafer to better understand the increase in mobility as a function of wafer number. These data sets are included in the Supplemental Material [26]. In Fig. 2(d), we plot the concentration of oxygen atoms at the QW, N_o, for each wafer. For wafers 1 to 11, N_o decreases from 8.7×10^{18}/cm^3 to the SIMS detection threshold of 1×10^{17}/cm^3. The steady decrease of oxygen content with increasing wafer number is likely due to reduced background in the reactor after the transfer of the wafers from the load lock to the growth chamber. The decrease in oxygen concentration is also correlated with the increase in mobility observed in Figs. 2(b) and 2(c). Wafer 26, which marks the beginning of a second cassette of wafers, shows an abrupt increase in N_o, which is also correlated with a drop in the mobility. The combination of mobility and SIMS data suggest that oxygen contamination is a mobility limiting factor in these undoped Si/SiGe heterostructures. A similar correlation has been observed in undoped Si/SiGe heterostructures grown by molecular-beam epitaxy [27].

In addition to the correlation between N_o and μ, the data show that the heterostructure growth profile impacts the mobility of samples later in the growth series. As h is increased from 40 to 50 nm for wafers 15 and 16, we observe a corresponding increase in μ_H and μ_L. For wafers 16 through 19,

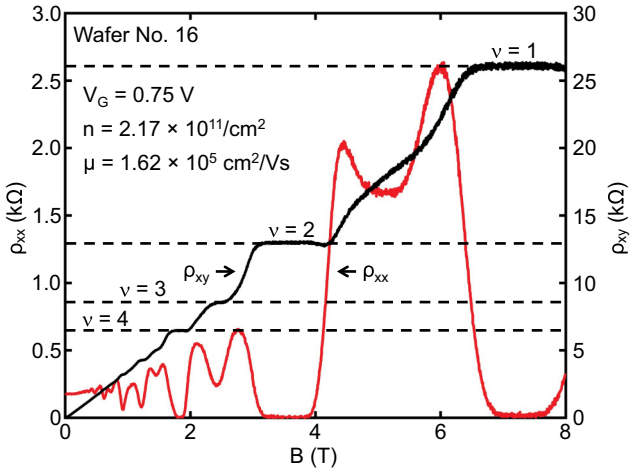

FIG. 3. (Color online) Wafer 16. ρ_{xx} (red) and ρ_{xy} (black) as a function of B, with $V_G = 0.75$ V and $T = 0.35$ K. We observe clear quantum Hall plateaus in ρ_{xy} at integer filling factors ν for $B > 1.5$ T.

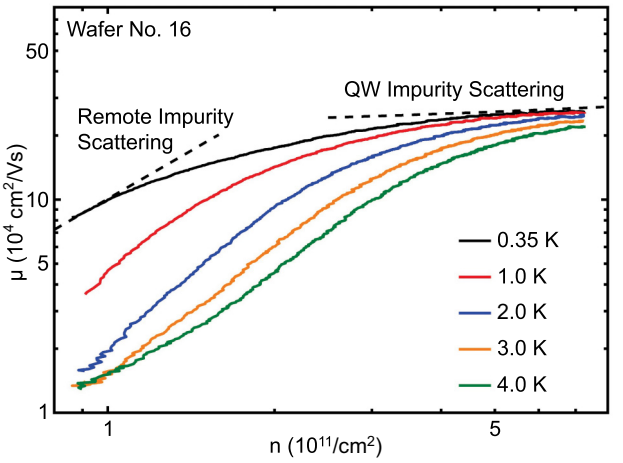

FIG. 4. (Color online) Wafer 16. $\mu(n)$ for five different temperatures. The dashed lines show the predicted slopes for remote ionized impurity scattering and scattering due to impurities in the QW [13]. The charged impurity densities used to produce the two dashed lines are 3.7×10^{12}/cm^2 at a distance of 50 nm from the QW center (where the Al_2O_3/Si interface is) for remote impurity scattering, and 3.4×10^{9}/cm^2 in the QW center.

h is constant and both μ_H and μ_L show very little variation. At wafer 20, h undergoes a large decrease from 50 to 20 nm, which is correlated with a large drop in mobility. For wafers 20 through 25, h increases from 20 to 50 nm and we see that the mobilities also recover to the values obtained from wafer 19. In contrast, for lower wafer numbers, the correlations between h and mobility are weaker, suggesting that N_o is the dominant mobility limiting mechanism in these wafers. To obtain a better quantitative understanding of these correlations, we perform detailed measurements on wafers 5 and 16 at $T = 0.35$ K in order to contrast the properties of a low- and high-mobility wafer.

IV. HIGH-MOBILITY SAMPLE

Based on its high 4.2 K mobility, a Hall bar from wafer 16 was cooled down in a ^{3}He cryostat for further study. The oxygen content at the QW is $N_o = 5.0\times10^{17}$/cm^3 [26]. Figure 3 shows ρ_{xx} and ρ_{xy} as a function of B up to 8 T, with $n = 2.17\times10^{11}$/cm^2. From the low-field magnetotransport data, we extract $\mu = 1.62\times10^5$ cm^2/Vs. We observe quantum Hall plateaus in ρ_{xy} at consecutive integer filling factors ν for $B > 1.5$ T, which indicates that both spin and valley degeneracies are lifted. In addition, ρ_{xx} displays clear zeros, ruling out parallel conduction paths. For $\nu > 6$, plateaus in ρ_{xy} are no longer visible, although oscillations in ρ_{xx} are visible up to $\nu = 24$.

Figure 4 shows μ as a function of n at five temperatures. At $T = 0.35$ K, $\mu(n)$ is not well described by a single exponent, an often observed feature in 2DEG systems [17]. Our data differ from previous work [23], where an exponent of $\alpha = 1.7$ is observed in the density range of $n = 0.6$–4.5×10^{11}/cm^2. For $n < 1\times10^{11}$/cm^2, the data roughly follow a $\mu \propto n^{1.5}$ scaling, consistent with scattering due to remote charged impurities [13]. At higher n, μ increases more slowly and nearly saturates when $n > 5\times10^{11}$/cm^2. The high-density saturation likely arises from impurity charges located very near or inside the QW, which lead to values of μ that are only weakly dependent on n [13]. It is notable that the mobility curves are temperature dependent at low densities, but all saturate to nearly the same high-density value of 250 000 cm^2/Vs. Another feature of the higher-temperature data is that the density dependence of $\mu(n)$ becomes stronger, though the curvature persists up to 4 K. At $T = 4$ K, the data approximately follow a $\mu \propto n^{1.5}$ trend for $n < 3\times10^{11}$/cm^2.

To further probe the scattering mechanisms that limit the mobility of wafer 16, we measure low-field SdH oscillations in the longitudinal resistivity, ρ_{xx}. We subtract the slowly varying background ρ_b from ρ_{xx} as outlined by Coleridge *et al.* [18], yielding $\Delta\rho_{xx} = \rho_{xx} - \rho_b$. $\Delta\rho_{xx}$ is plotted against $1/B$ for three densities in Fig. 5(a). Clear periodic oscillations are observed, with a periodicity of 4 in ν. This is consistent with the twofold spin degeneracy and twofold valley degeneracy at low fields. At higher fields $B > 0.7$ T, splitting of the peak in each period of the SdH oscillation becomes visible, due to increased Zeeman splitting. This splitting is examined in detail in Sec. VIII. We extract the amplitude of the oscillations in $\Delta\rho_{xx}$ at each period in $1/B$ [28] which is fit to

$$\Delta\rho_{xx} = 4\rho_0 X(T)\exp(-\pi/\omega_c\tau_q), \quad (1)$$

where τ_q is the quantum lifetime of the electrons, ρ_0 is the zero-field resistivity, $X(T) = (2\pi^2 k_B T/\hbar\omega_c)/\sinh(2\pi^2 k_B T/\hbar\omega_c)$ is the temperature-damping factor, $\omega_c = eB/m^*$ is the cyclotron frequency, and k_B is the Boltzmann's constant. We use a constant effective mass $m^* = 0.2m_e$, where m_e is the free-electron mass, for all fits [29]. Figure 5(b) shows the results of such fits, known as Dingle plots. The slopes of the Dingle plots [19] are inversely proportional to the quantum lifetime τ_q and imply shorter quantum lifetimes at lower densities.

In Fig. 5(c), we compare the transport lifetime τ_t and the quantum lifetime τ_q across the electron density range $n = 1.8$–6.8×10^{11}/cm^2. Values of τ_t are obtained [30] from the mobility data in Fig. 4 via $\tau_t = \mu m^*/e$ and values of τ_q are

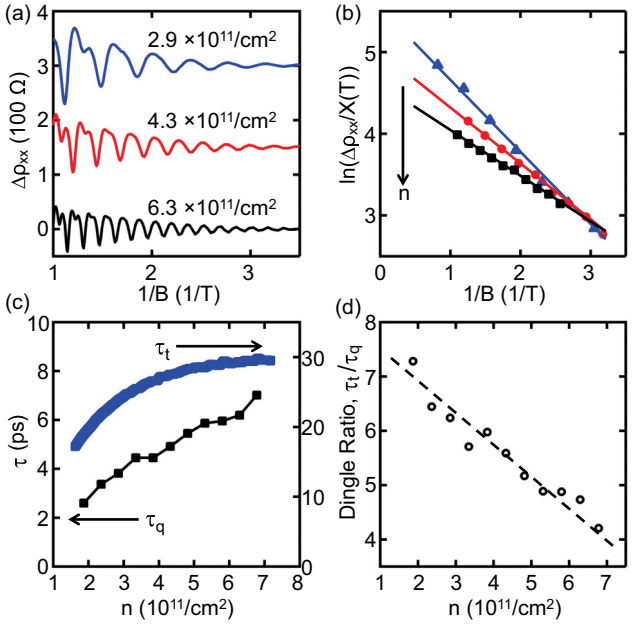

FIG. 5. (Color online) Wafer 16. (a) $\Delta\rho_{xx}$ as a function of $1/B$ for three electron densities at $T = 0.4$ K. Traces have been offset by 150 Ω for clarity. (b) Dingle plots for the data in (a). Values of $\Delta\rho_{xx}$ used in this plot are the average of the maximum and minimum of each period of the SdH oscillations shown in (a). (c) τ_q and τ_t as functions of n at $T = 0.4$ K. (d) Dingle ratio τ_t/τ_q as a function of n at $T = 0.4$ K. The dashed line is a guide to the eye.

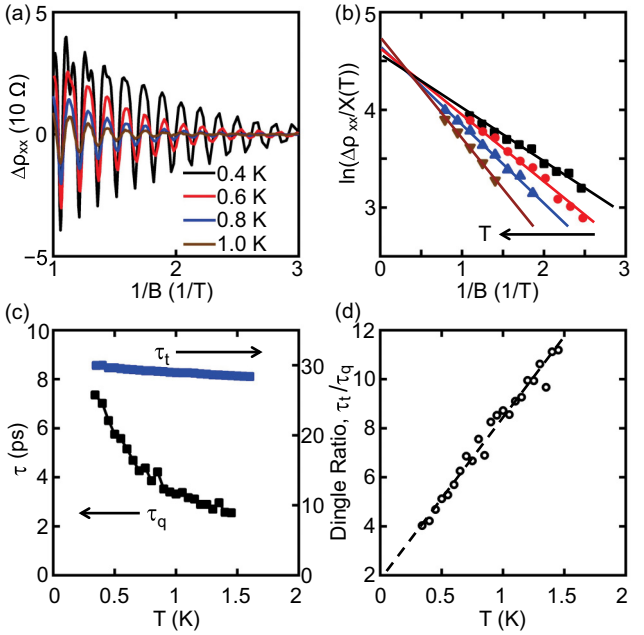

FIG. 6. (Color online) Wafer 16. (a) $\Delta\rho_{xx}$ as a function of $1/B$ for $n = 6.7\times10^{11}/\text{cm}^2$ at four different temperatures. (b) Dingle plots for the data shown in (a). (c) τ_q and τ_t as a function of T at $n = 6.7\times10^{11}/\text{cm}^2$. (d) Dingle ratio as a function of T. The dashed line is a guide to the eye.

obtained from analysis of the low-field SdH oscillations. Both lifetimes show similar dependencies on n, and Dingle ratios, defined as τ_t/τ_q, range from 4 to 7, as shown in Fig. 5(d). In comparison with previous work on GaAs/AlGaAs [19] and modulation-doped SiGe [21] where the Dingle ratios typically range from 10 to 20, the Dingle ratios measured for this undoped sample are sizably smaller, indicating that large-angle scattering plays a more dominant role in this sample. Such a situation would arise when the distribution of impurities is more concentrated towards the location of the 2DEG [13]. This is unexpected in an undoped system where charged impurities are thought to reside mostly in the Al_2O_3/Si interface [23], ∼50 nm away from the 2DEG in this sample. Our interpretation of the possible cause for such distribution is the peak in oxygen impurities at the 2DEG location [26]. Ionization of a small fraction of these oxygen atoms would lead to a sizable amount of impurity charges inside the QW, which contribute to large-angle scattering with a Dingle ratio near unity. The decreasing trend of the Dingle ratio at higher densities also differs from theoretical calculations based on a single dopant sheet [15]. This deviation is interpreted to be due to the mitigated contribution of remote impurity scattering to the overall momentum scattering rate at higher densities, since the scattering rate $\tau_t^{-1} \propto n^{-1.5}$ for remote impurities, but $\tau_t^{-1} \propto n^{-0.1}$ for impurities inside the QW. At higher densities, scattering from impurities inside the QW becomes more dominant than remote impurities, which reduces the overall Dingle ratio.

The quantum lifetime τ_q for this high-mobility sample is also measured as a function of T at $n = 6.7\times10^{11}/\text{cm}^2$. Figures 6(a) and 6(b) display low-field SdH oscillations and the associated Dingle plots. The extracted values of τ_q are plotted alongside τ_t, obtained by measuring the temperature-dependent mobility at this density [Fig. 6(c)]. The transport lifetime is relatively insensitive to temperature, while the quantum lifetime varies by nearly a factor of 4 from $T = 0.4$ to 1.5 K. The resulting Dingle ratio, plotted in Fig. 6(d), increases almost linearly with temperature from 4 to 11. These data are in contrast with a single-particle description of electron scattering in 2DEGs [14,15,31], where the temperature dependence of both lifetimes is expected to be weak in the $T \ll T_F$ regime, where T_F is the Fermi temperature (approximately 47 K at this density).

Arapov *et al.* [32] have recently measured an InGaA/GaAs double QW structure and report a similar, strong temperature dependence of τ_q at $T \ll T_F$, which the authors attribute to electron-electron interactions. A similar mechanism may explain the trends observed in this work. While electron-electron interactions may be significant, our analysis is based on the established single-particle model due to the fact that electron-electron interactions are expected to renormalize both τ_q and m^* [33,34]. The observed temperature dependence of τ_q in Fig. 6(c) could be due to a change in τ_q with temperature or an apparent change in τ_q due to a renormalized m^*. It is difficult to distinguish between these two possibilities based on the SdH data alone.

V. LOW-MOBILITY SAMPLE

We next examine data from wafer 5, which has a much lower maximum mobility of $\mu = 7.5\times10^4$ cm^2/Vs at 4.2 K. Wafer 5 has a 2-nm-thick Si cap, a ($h = 40$)-nm-thick SiGe

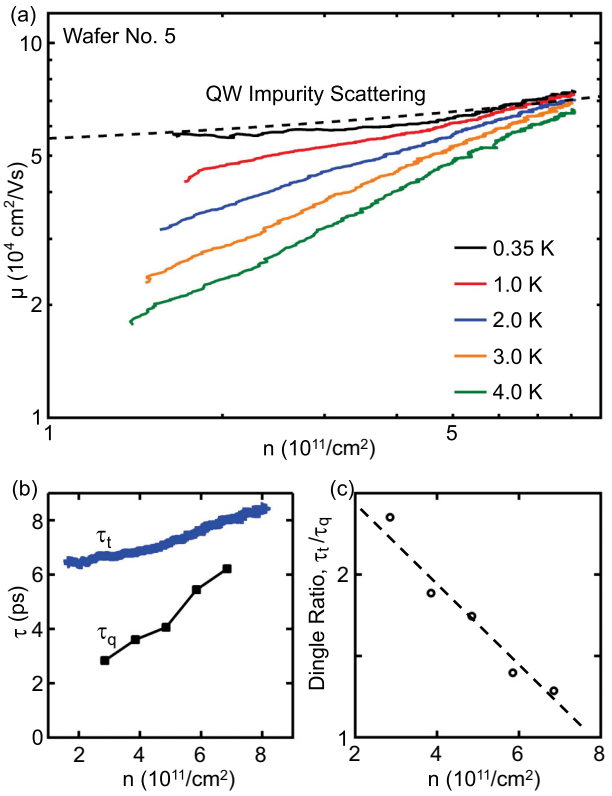

FIG. 7. (Color online) Wafer 5 (low-mobility sample). (a) $\mu(n)$ at five different temperatures. The dashed line shows the prediction for scattering from impurities in the QW with a charged impurity density of 1.3×10^{10}/cm^2 at the QW center. (b) τ_q and τ_t plotted as a function of n, extracted from low-field SdH oscillations. $T = 0.4$ K in this plot. (c) Dingle ratios τ_t/τ_q obtained from the data in (b).

spacer layer, and a 5-nm-wide Si QW. SIMS analysis shows a similar distribution of oxygen inside the SiGe spacer as the high-mobility sample [26]. However, the oxygen content in the QW is peaked at $N_o = 2.5\times10^{18}$/cm^3, which is five times higher than the high-mobility sample.

Figure 7 shows the results of magnetotransport measurements on this low-mobility sample. $\mu(n)$ is plotted in Fig. 7(a) and increases with n, although with a weaker dependence than the high-mobility sample. $\mu(n)$ is also temperature dependent, and more strongly scales with n at higher temperatures. At $T = 0.35$ K, $\mu(n)$ is nearly density independent. As T increases, $\mu(n)$ becomes more density dependent and eventually reaches an approximate scaling of $\mu \propto n^{0.7}$ at $T = 4$ K. The smaller power-law exponent for this sample suggests that remote impurity scattering plays a less significant role compared to the high-mobility sample. Instead, electron scattering is likely dominated by impurity charges situated inside the QW, which is consistent with the higher oxygen content observed in the SIMS data [26].

Figure 7(b) shows τ_q and τ_t for the low-mobility sample at five different densities and with $T = 0.4$ K. Both lifetimes are shorter at lower electron densities, similar to the high-mobility sample. Despite the factor of ~3 difference in τ_t between the two samples, the values of τ_q are very similar. This observation agrees well with recent theoretical results by Das Sarma *et al.* [35], who considered a two-impurity model and showed that increasing (decreasing) τ_t does not necessarily lead to increasing (decreasing) τ_q when there is more than one scattering mechanism. We also plot the density-dependent Dingle ratio τ_t/τ_q of this sample in Fig. 7(c). τ_t/τ_q ranges from 1.3 at high density to 2.3 at low density, significantly smaller than the high-mobility sample. The smaller Dingle ratio observed in this sample implies that the underlying scattering events are even larger in angle compared to the high-mobility sample, consistent with scattering from QW impurities.

VI. ESTIMATE OF DEFECT DENSITIES

Monroe *et al.* have carefully analyzed seven scattering mechanisms that are potentially relevant to the Si/SiGe materials system [13]. Among these mechanisms, alloy scattering, scattering due to strain modulation, scattering due to vicinal surfaces, and scattering from threading dislocations are estimated to limit mobilities to above 10^7 cm^2/Vs, which is two orders of magnitude higher than the mobilities measured in our samples. Interface roughness has been reported to be an important factor in a ~500-nm-deep Si/SiGe QW structure [24], but is expected to lead to a mobility that decreases with increasing density (a trend that is not observed in our data). We therefore limit our analysis to the two remaining scattering mechanisms: remote impurity scattering from charges located at the Al_2O_3/Si interface and scattering from oxygen-related background charges in the QW.

We now compare the experimental data with these predictions, starting with the high-mobility sample. Figure 4 shows $\mu(n)$ for wafer 16. At low densities, $\mu(n)$ roughly follows the $\mu \propto n^{1.5}$ power law expected for remote impurity scattering, while for higher densities μ is a weak function of n. Superimposed on the data are dashed lines showing the expected scaling for remote impurity scattering and scattering from impurities in the QW calculated using theoretical results of Monroe *et al.* We set the distance between the remote impurities and the 2DEG to be $h = 50$ nm such that the remote impurities are Al_2O_3/Si interface charges, as reported by Li *et al.* [23]. The 2D remote impurity density is adjusted to $n_1 = 3.7\times10^{12}$/cm^2 to bring theory into agreement with the data. Similarly, for scattering from impurities in the QW, we find reasonable agreement with the data when the 2D QW impurity density $n_2 = 3.4\times10^9$/cm^2. Dingle ratio data for wafer 16 are plotted in Fig. 5(d) and show a linear decrease with n over the entire density range. This is broadly consistent with a crossover from remote impurity scattering-limited transport to local defect scattering-limited transport as n increases.

In comparison, $\mu(n)$ is shown for the low-mobility sample (wafer 5) in Fig. 7(a). At $T = 0.35$ K, the mobility is weakly dependent on density over the entire density range, consistent with scattering from impurities in the QW. The dashed line shows the prediction for scattering from impurities in the QW taking $n_2 = 1.3\times10^{10}$/cm^2. We note that this defect density is four times higher than the high-mobility sample, reminiscent of the factor of 5 difference between the oxygen contents in the QWs of the low- and high-mobility samples [26]. It is also clear that the Dingle ratio is much less sensitive to density, with $\tau_t/\tau_q \sim 1$–2 over the entire density range. The small Dingle ratio is consistent with scattering from impurities in the QW.

VII. METAL-TO-INSULATOR TRANSITION

For spin-based quantum information processing, quantum dots are typically operated in the few-electron regime [12]. One important gauge for the degree of disorder at low electron density is the critical electron density, n_c, for the metal-to-insulator transition (MIT) in 2DEGs. For silicon, a MIT has been observed in MOSFETs [36,37], modulation-doped Si/SiGe structures [38–40], an undoped Si/SiGe 2DEG structure [41], and an ambipolar Si-vacuum FET [42]. Values of n_c vary greatly in Si/SiGe systems, ranging from 0.32 to $4.05\times10^{11}/\text{cm}^2$ [38–41].

The experimental signature for the MIT in 2DEG systems is a sign reversal in $d\rho/dT$, where ρ is the resistivity of the system [36]. For $n > n_c$, $d\rho/dT > 0$ and the 2DEG displays metallic behavior. For $n < n_c$, $d\rho/dT < 0$ and the 2DEG behaves as an insulator. In Fig. 8, we plot $\rho_{xx}(T)$ for the high-mobility sample at ten different densities below $n = 1.0\times10^{11}/\text{cm}^2$. We observe the following features in this data set:

(1) At the lowest two densities $n = 0.34\times10^{11}/\text{cm}^2$ and $0.36\times10^{11}/\text{cm}^2$, $d\rho_{xx}/dT < 0$ throughout the measured temperature range. In addition, ρ_{xx} appears to diverge exponentially at $T < 1$ K, indicative of a true insulating phase [43].

(2) At the next three higher densities, $n = 0.38$, 0.40, and $0.42\times10^{11}/\text{cm}^2$, ρ_{xx} varies nonmonotonically with temperature. While $d\rho_{xx}/dT < 0$ at $T = 4.2$ K, $d\rho_{xx}/dT > 0$ for a small, intermediate-temperature range. We note that this behavior has also been observed by Lu *et al.* in another undoped Si/SiGe sample [41], and is common in Si MOSFET systems [44].

(3) $d\rho_{xx}/dT > 0$ at 0.5 K for $n \geqslant n_c$, where $n_c = 0.46\times10^{11}/\text{cm}^2$.

(4) At $n \geqslant n_c$, with the exception of $n = 0.51\times10^{11}/\text{cm}^2$, $d\rho_{xx}/dT > 0$ up to a crossover temperature T_c. For $T > T_c$, $d\rho_{xx}/dT < 0$. Furthermore, T_c increases with increasing n. Das Sarma *et al.* interpreted this behavior as a quantum-to-classical crossover [14,43,45].

We note that the critical density is comparable to the lowest value of $0.32\times10^{11}/\text{cm}^2$ that has been reported in doped Si/SiGe structures [40], and a factor of 4 lower than the value of $1.9\times10^{11}/\text{cm}^2$ observed in a previous work on undoped Si/SiGe structure [41], indicating a very low level of disorder in our undoped sample. The critical density observed in our system lies at the lower end of the critical density spectrum [46] and within an order of magnitude of the lowest value of $n_c = 7.7\times10^9/\text{cm}^2$ in a GaAs system [47]. We have successfully measured few-electron charge stability diagrams for quantum dots fabricated from wafer 16 [48], which gives further evidence of a low disorder potential.

VIII. VALLEY SPLITTING

Another important figure of merit for the Si/SiGe quantum well system is the valley splitting. Measurements of the valley splitting in Si MOSFET systems have been extensively performed. Most values range from 0.7–1.5 meV [49,50], with one study reporting a value as large as 23 meV [51]. In comparison, the valley splitting in Si/SiGe systems tends to be smaller, ranging from 0.05–0.3 meV [52–54]. In this section, we determine Δ_v through careful analysis of the SdH oscillations in wafer 16.

In Fig. 9, we plot $\rho_{xx}(B)$ with $n = 6.6\times10^{11}/\text{cm}^2$. SdH oscillations are observed above an effective field $B_{\text{eff}} = 0.38$ T and have a periodicity of 4 in ν. For $B > B_s = 0.88$ T, we observe change in periodicity of the SdH oscillations, indicating that spin degeneracy has been lifted. The periodicity changes again beyond $B_v = 1.8$ T, consistent with the lifting of both spin and valley degeneracies. We have verified that the spin degeneracy is lifted before valley degeneracy using the tilted field method [52,53].

The energy spectrum of 2D electrons in a perpendicular field is described by four characteristic energy scales. The first is the Zeeman splitting, $E_z = g\mu_B B$, where μ_B is the Bohr magneton and g is the electronic g factor. The second is $E_1 = e\hbar B/m^* - E_z$, which is the Landau-level spacing minus the Zeeman splitting. The third is the valley splitting, Δ_v.

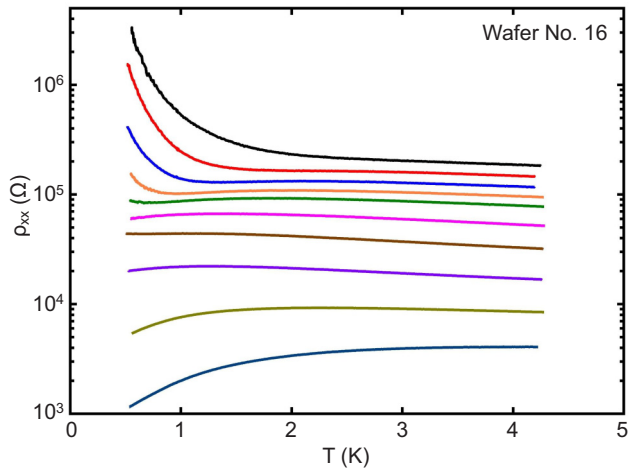

FIG. 8. (Color online) Wafer 16. $\rho_{xx}(T)$ at $B = 0$ T for $n = 0.34$, 0.36,0.38,0.40,0.42,0.46,0.51,0.59,0.73, and $0.96\times10^{11}/\text{cm}^2$ (from top to bottom). A metal-to-insulator transition occurs at $n_c = 0.46\times10^{11}/\text{cm}^2$.

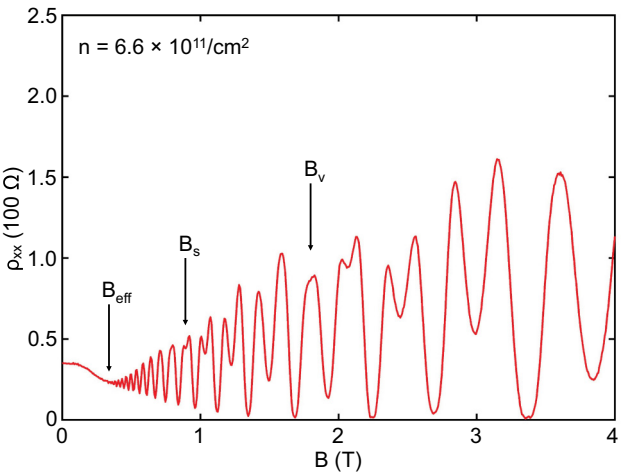

FIG. 9. (Color online) Wafer 16. $\rho_{xx}(B)$ at $T = 0.4$ K. SdH oscillations are observed beyond $B_{\text{eff}} = 0.38$ T. Spin (valley) degeneracy is lifted at $B_s = 0.88$ T ($B_v = 1.8$ T).

Finally, clear SdH oscillations will only be observed when the Landau-level spacing is greater than the Landau-level broadening $\Gamma \approx \hbar/2\tau_q$. Spin splitting becomes visible when $E_z(B_s) \approx \Gamma$. Based on the effective field at which the SdH oscillations become visible, we estimate $\Gamma \approx E_l(B_{\rm eff})$. We then have the relation $E_z(B_s) \approx E_l(B_{\rm eff})$, allowing us to extract $g = 3.0 \pm 0.2$. The g factor is in reasonable agreement with the value of $g = 2.9 \pm 0.1$ at $n = 5.9\times10^{11}/{\rm cm}^2$ found in a previous study [53]. Based on this experimental value of g, we find $\Gamma \sim 150 \pm 10\,\mu$eV. Finally, the valley degeneracy is lifted at the field for which $\Delta_v\,(B = 1.8\ {\rm T}) \sim 150\ \mu$eV. The valley splitting is substantial and comparable to the two-electron singlet-triplet splitting that is measured in GaAs quantum dots [3,4].

IX. CONCLUSIONS

We have measured 26 wafers with different growth parameters to identify the dominant mobility limiting mechanisms in undoped Si/SiGe QW heterostructures. At 4.2 K, we find correlations between mobility and oxygen content at the QW as well as the thickness of the top SiGe spacer. We also measured τ_t and τ_q for two Si/SiGe QW heterostructures across a wide density range at $T \sim 0.35$ K. Based on the density dependencies of the two lifetimes, we conclude that the mobility of high-quality samples with low oxygen content at the QW is mostly limited by remote impurity charges, while the lower-mobility samples with high oxygen content in the QW are limited by the impurity charges inside or very close to the QW, consistent with the correlations observed at 4.2 K. To further assess the merits of the high-mobility heterostructure as a platform for spin-based quantum dots, we have measured a low critical density $n_c = 0.46\times10^{11}/{\rm cm}^2$ for the MIT and a valley splitting $\Delta_v \sim 150\ \mu$eV.

While we cannot rule out effects due to other impurities, our SIMS results suggest that significant improvements in the electron mobility may be obtained by reducing the level of oxygen content in the Si/SiGe heterostructure. Our data give no information about the microscopic scattering mechanism that results from the oxygen impurities. The literature suggests several possibilities: (a) lattice strain due to interstitial and substitutional oxygen [55], (b) thermal donor generation [56], and (c) enhanced donor generation rate due to the presence of carbon impurities [57]. Further work is needed to identify the mechanism that leads to the correlation between oxygen concentration and mobility.

The SiGe spacer layer thickness can also be increased to reduce scattering from charged impurities at the surface of the wafer. This second approach has limitations for quantum dot devices, as it is desirable to have strong in-plane electrostatic confinement, which is harder to obtain in samples with deeper QWs. The magnetic fields at which the valley splitting was extracted corresponds to a cyclotron radius of ∼20 nm, which is a realistic size for the lithographic patterning of quantum dots on Si. Therefore, efforts should also be directed towards reducing the size of Si quantum dots to emulate high levels of magnetic confinement, which yielded large values of valley splitting in this work. Overlapping gate architectures may prove helpful to achieve tight electronic confinement in the relatively high-effective-mass Si/SiGe quantum well system [48].

ACKNOWLEDGMENTS

We thank S. Das Sarma and M. Shayegan for valuable discussions. Research was sponsored by ARO Grant No. W911NF-15-1-0149 with partial support from the NSF (Grants No. DMR-1409556 and No. DMR-1420541).

[1] K. Saeedi, S. Simmons, J. Z. Salvail, P. Dluhy, H. Riemann, N. V. Abrosimov, P. Becker, H.-J. Pohl, J. J. L. Morton, and M. L. W. Thewalt, Science **342**, 830 (2013).
[2] M. A. Eriksson, M. Friesen, S. N. Coppersmith, R. Joynt, L. J. Klein, K. Slinker, C. Tahan, P. M. Mooney, J. O. Chu, and S. Koester, Quantum Inf. Proc. **3**, 133 (2004).
[3] J. R. Petta, A. C. Johnson, J. M. Taylor, E. A. Laird, A. Yacoby, M. D. Lukin, C. M. Marcus, M. P. Hanson, and A. C. Gossard, Science **309**, 2180 (2005).
[4] R. Hanson, L. P. Kouwenhoven, J. R. Petta, S. Tarucha, and L. M. K. Vandersypen, Rev. Mod. Phys. **79**, 1217 (2007).
[5] L. J. Klein, K. A. Slinker, J. L. Truitt, S. Goswami, K. L. M. Lewis, S. N. Coppersmith, D. W. van der Weide, M. Friesen, R. H. Blick, D. E. Savage, M. G. Lagally, C. Tahan, R. Joynt, M. A. Eriksson, J. O. Chu, J. A. Ott, and P. M. Mooney, Appl. Phys. Lett. **84**, 4047 (2004).
[6] N. Shaji, C. B. Simmons, M. Thalakulam, L. J. Klein, H. Qin, H. Luo, D. E. Savage, M. G. Lagally, A. J. Rimberg, R. Joynt, M. Friesen, R. H. Blick, S. N. Coppersmith, and M. A. Eriksson, Nat. Phys. **4**, 540 (2008).
[7] K. A. Slinker, K. L. M. Lewis, C. C. Haselby, S. Goswami, L. J. Klein, J. O. Chu, S. N. Coppersmith, R. Joynt, R. H. Blick, M. Friesen, and M. A Eriksson, New J. Phys. **7**, 246 (2005).
[8] C. Payette, K. Wang, P. J. Koppinen, Y. Dovzhenko, J. C. Sturm, and J. R. Petta, Appl. Phys. Lett. **100**, 043508 (2012).
[9] T. M. Lu, N. C. Bishop, T. Pluym, J. Means, P. G. Kotula, J. Cederberg, L. A. Tracy, J. Dominguez, M. P. Lilly, and M. S. Carroll, Appl. Phys. Lett. **99**, 043101 (2011).
[10] M. G. Borselli, K. Eng, E. T. Croke, B. M. Maune, B. Huang, R. S. Ross, A. A. Kiselev, P. W. Deelman, I. Alvarado-Rodriguez, A. E. Schmitz, M. Sokolich, K. S. Holabird, T. M. Hazard, M. F. Gyure, and A. T. Hunter, Appl. Phys. Lett. **99**, 063109 (2011).
[11] K. Wang, C. Payette, Y. Dovzhenko, P. W. Deelman, and J. R. Petta, Phys. Rev. Lett. **111**, 046801 (2013).
[12] B. M. Maune, M. G. Borselli, B. Huang, T. D. Ladd, P. W. Deelman, K. S. Holabird, A. A. Kiselev, I. Alvarado-Rodriguez, R. S. Ross, A. E. Schmitz, M. Sokolich, C. A. Watson, M. F. Gyure, and A. T. Hunter, Nature (London) **481**, 344 (2012).
[13] D. Monroe, Y. H. Xie, E. A. Fitzgerald, P. J. Silverman, and G. P. Watson, J. Vac. Sci. Technol. B **11**, 1731 (1993).
[14] E. H. Hwang and S. Das Sarma, Phys. Rev. B **72**, 085455 (2005).
[15] S. Das Sarma and F. Stern, Phys. Rev. B **32**, 8442 (1985).
[16] M. Shayegan, V. J. Goldman, C. Jiang, T. Sajoto, and M. Santos, Appl. Phys. Lett. **52**, 1086 (1988).
[17] C. Jiang, D. C. Tsui, and G. Weimann, Appl. Phys. Lett. **53**, 1533 (1988).

[18] P. T. Coleridge, Semicond. Sci. Technol. **5**, 961 (1990).
[19] P. T. Coleridge, Phys. Rev. B **44**, 3793 (1991).
[20] K. Chain, J. H. Huang, J. Duster, P. K. Ko, and C. Hu, Semicond. Sci. Technol. **12**, 355 (1997).
[21] K. Ismail, M. Arafa, K. L. Saenger, J. O. Chu, and B. S. Meyerson, Appl. Phys. Lett. **66**, 1077 (1995).
[22] N. Sugii, K. Nakagawa, Y. Kimura, S. Yamaguchi, and M. Miyao, Semicond. Sci. Technol. **13**, A140 (1998).
[23] J.-Y. Li, C.-T. Huang, L. P. Rokhinson, and J. C. Sturm, Appl. Phys. Lett. **103**, 162105 (2013).
[24] S.-H. Huang, T.-M. Lu, S.-C. Lu, C.-H. Lee, C. W. Liu, and D. C. Tsui, Appl. Phys. Lett. **101**, 042111 (2012).
[25] T. M. Lu, C.-H. Lee, S.-H. Huang, D. C. Tsui, and C. W. Liu, Appl. Phys. Lett. **99**, 153510 (2011).
[26] See Supplemental Material at http://link.aps.org/supplemental/10.1103/PhysRevB.92.035304 for SIMS data from wafers 5 and 16.
[27] C. J. K. Richardson (private communication).
[28] M. Padmanabhan, T. Gokmen, N. C. Bishop, and M. Shayegan, Phys. Rev. Lett. **101**, 026402 (2008).
[29] F. Schäffler, Semicond. Sci. Technol. **12**, 1515 (1997).
[30] N. Ashcroft and N. Mermin, *Solid State Physics* (Saunders College, Rochester, NY, 1976).
[31] T. Ando, A. B. Fowler, and F. Stern, Rev. Mod. Phys. **54**, 437 (1982).
[32] Y. G. Arapov, S. V. Gudina, V. N. Neverov, S. M. Podgornykh, and M. V. Yakunin, Low Temp. Phys. **39**, 43 (2013).
[33] Y.-W. Tan, J. Zhu, H. L. Stormer, L. N. Pfeiffer, K. W. Baldwin, and K. W. West, Phys. Rev. Lett. **94**, 016405 (2005).
[34] Y. Zhang and S. Das Sarma, Phys. Rev. B **72**, 075308 (2005).
[35] S. Das Sarma and E. H. Hwang, Phys. Rev. B **90**, 035425 (2014).
[36] S. V. Kravchenko, G. V. Kravchenko, J. E. Furneaux, V. M. Pudalov, and M. D'Iorio, Phys. Rev. B **50**, 8039 (1994).
[37] D. Popović, A. B. Fowler, and S. Washburn, Phys. Rev. Lett. **79**, 1543 (1997).
[38] K. Lai, W. Pan, D. C. Tsui, and Y.-H. Xie, Appl. Phys. Lett. **84**, 302 (2004).
[39] E. B. Olshanetsky, V. Renard, Z. D. Kvon, J. C. Portal, N. J. Woods, J. Zhang, and J. J. Harris, Phys. Rev. B **68**, 085304 (2003).
[40] K. Lai, W. Pan, D. C. Tsui, S. A. Lyon, M. Mühlberger, and F. Schäffler, Phys. Rev. B **72**, 081313 (2005).
[41] T. M. Lu, J. Liu, J. Kim, K. Lai, D. C. Tsui, and Y. H. Xie, Appl. Phys. Lett. **90**, 182114 (2007).
[42] B. Hu, M. M. Yazdanpanah, B. E. Kane, E. H. Hwang, and S. Das Sarma, arXiv:1502.02956.
[43] S. Das Sarma and E. H. Hwang, Phys. Rev. B **68**, 195315 (2003).
[44] S. Das Sarma, E. H. Hwang, K. Kechedzhi, and L. A. Tracy, Phys. Rev. B **90**, 125410 (2014).
[45] S. Das Sarma and E. H. Hwang, Phys. Rev. B **69**, 195305 (2004).
[46] M. P. Sarachik, Europhys. Lett. **57**, 546 (2002).
[47] J. Yoon, C. C. Li, D. Shahar, D. C. Tsui, and M. Shayegan, Phys. Rev. Lett. **84**, 4421 (2000).
[48] D. M. Zajac, T. M. Hazard, X. Mi, K. Wang, and J. R. Petta, Appl. Phys. Lett. **106**, 223507 (2015).
[49] H. Köhler and M. Roos, Phys. Status Solidi B **91**, 233 (1979).
[50] V. M. Pudalov, S. G. Semenchinskii, and V. S. Édel'Man, JETP Lett. **41**, 325 (1985).
[51] K. Takashina, Y. Ono, A. Fujiwara, Y. Takahashi, and Y. Hirayama, Phys. Rev. Lett. **96**, 236801 (2006).
[52] P. Weitz, R. Haug, K. von. Klitzing, and F. Schäffler, Surf. Sci. **361**, 542 (1996).
[53] S. J. Koester, K. Ismail, and J. O. Chu, Semicond. Sci. Technol. **12**, 384 (1997).
[54] S. Goswami, K. A. Slinker, M. Friesen, L. M. McGuire, J. L. Truitt, C. Tahan, L. J. Klein, J. O. Chu, P. M. Mooney, D. W. van der Weide, R. Joynt, S. N. Coppersmith, and M. A. Eriksson, Nat. Phys. **3**, 41 (2007).
[55] W. Bond and W. Kaiser, J. Phys. Chem. Solids **16**, 44 (1960).
[56] V. Cazcarra and P. Zunino, J. Appl. Phys. **51**, 4206 (1980).
[57] A. Kanamori and M. Kanamori, J. Appl. Phys. **50**, 8095 (1979).